Data-Driven Identification unravels multiaxial mechanical response of a carbon-black filled elastomer during ageing

H. Madeira, L. Costecalde, Michel Coret, A. Leygue, Pierre Yves Le Gac, M. Le Gall, E. Verron

Polymer Testing 137 (2024) 108521

Contents lists available at ScienceDirect

Polymer Testing

journal homepage: www.elsevier.com/locate/polytest

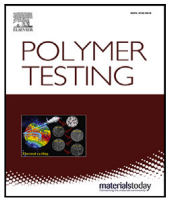

Data-Driven Identification unravels multiaxial mechanical response of a carbon-black filled elastomer during ageing

H. Madeira [a,b,*], L. Costecalde [a], M. Coret [a], A. Leygue [a], P.Y. Le Gac [b], M. Le Gall [b], E. Verron [a]

[a] Nantes Université, Ecole Centrale de Nantes, CNRS, GeM, UMR 6183, F-44000 Nantes, France
[b] Ifremer, RDT Research and Technological Development Unit, F-29280 Plouzané, France

ARTICLE INFO

Keywords:
Elastomer
Multiaxiality
Ageing
Data-driven
Strain energy density

ABSTRACT

Under environmental exposure, the mechanical properties of elastomers change due to ageing, all while enduring mechanical service loading conditions. The influence of ageing on the multiaxial mechanical response of elastomers remains an understudied question, lacking exploration in both experimental evidence and modelling proposals. The present study describes an experimental/numerical approach to characterize the multiaxial behaviour of elastomers with consideration of ageing. This technique associates complex experimental tests conducted with a hexapod device, with a Data-Driven Identification (DDI) algorithm. Practically, heterogeneous strain fields are measured by Digital Image Correlation (DIC), and the corresponding stress and energy fields are calculated by DDI. These fields are visualized through three-dimensional maps, encompassing kinematical quantities and strain energy density. These maps convincingly capture the stiffening induced by ageing, in different deformation modes. Finally, the coupling between ageing and multiaxiality is foregathered in a material database that can be fitted for further modelling purposes.

1. Introduction

The unique mechanical properties of elastomers render them essential components in a very broad spectrum of industries. Their high extensibility and dynamic properties are especially appreciated in structural engineering for many components such as membranes, seals, or springs [1–4]. In service, these parts are subjected to a wide diversity of loading conditions, straining them in various deformation modes [5,6]. The intricate interactions of these loading scenarios highlight the necessity of understanding and modelling the multiaxial mechanical response of these materials. On a larger time scale, when exposed to environmental conditions, elastomers undergo physical and/or chemical ageing, that impacts their overall durability. Thus, accurately predicting the service life of these components relies on integrating ageing effects into mechanical models. In this context, we are confronted to a dual and coupled issue: how is it possible to characterize the multiaxial mechanical behaviour of elastomers while simultaneously considering ageing effects?

Thermo-oxidative ageing of elastomers has been extensively studied since the 1950s [7,8], with a particular attention in the last few decades [9,10]. In polychloroprene rubber (CR), the most important degradation mechanism is well-established with a particularity: radical reactions oxidize the double bond, creating new crosslinks [11,12]. As this chemical process goes on, the length of elastically active chains reduces, hampering the mobility of the macromolecules. At the macroscopic scale, two discernible effects are observed under quasi-static loading conditions: a significant strain-stiffening of the material and a concurrent reduction in ultimate extensibility, both well-documented in numerous studies dedicated to the uniaxial tension of aged CR [13–15]. The macromolecular network degradation induces additional consequences on dynamic properties [16], especially for fatigue lifetime [17,18]. Despite the wealth of research in this domain, a pervasive limitation is the predominant focus on uniaxial tension when studying aged materials. This limitation is due to the challenge of experimental capabilities when dealing with ageing. Yet, this prevalent proceeding leaves a void in our understanding, particularly regarding the coupling between ageing and multiaxiality in the mechanical response.

Studies that consider the response of elastomers subjected to multiaxial loading conditions can be categorized into quasi-static and dynamic investigations. Although the literature provides extensive research on multiaxial fatigue [19–21], dynamics falls outside the scope of the present paper. The predominant approach in multiaxial quasi-static research involves performing multiple standard mechanical tests

* Corresponding author at: Nantes Université, Ecole Centrale de Nantes, CNRS, GeM, UMR 6183, F-44000 Nantes, France.
E-mail addresses: hugo.madeira@ec-nantes.fr (H. Madeira), lena.costecalde@gmail.com (L. Costecalde), michel.coret@ec-nantes.fr (M. Coret), adrien.leygue@ec-nantes.fr (A. Leygue), pierre.yves.le.gac@ifremer.fr (P.Y. Le Gac), maelenn.le.gall@ifremer.fr (M. Le Gall), erwan.verron@ec-nantes.fr (E. Verron).

https://doi.org/10.1016/j.polymertesting.2024.108521
Received 21 March 2024; Received in revised form 9 July 2024; Accepted 18 July 2024
Available online 20 July 2024

such as uniaxial, pure shear, and equibiaxial tensile deformation [22,23]. Then, constitutive law's parameters are identified to fit experimental data, which often yields to a satisfactory description of the material response [24,25]. Finely fitting experimental data across all deformation modes requires elaborate constitutive laws, usually with numerous parameters [26,27], that can accurately describe the material behaviour [28,29]. However, extrapolations are used to predict the behaviour under non-standard loading conditions, demanding not only a high level of confidence when choosing the constitutive law but also reliable experimental data. A rising way to complement classical approaches, aiming to help overcoming the corresponding limitations consists in using a data-driven identification algorithm [30]. This method, initially validated with synthetic data [31], has been further developed and advanced to construct the material database experimentally [32], for now at moderate strain levels. Practically, digital image correlation (DIC) technique measures a large series of heterogeneous strain fields, then it is coupled with the DDI algorithm to yield both stress and strain energy density fields. Appropriate graphical representations can then be employed to visualize and analyse these intricate datasets [33].

The adaptability of extending this method to three-dimensional loads is a valuable asset in characterizing elastomer materials, since it provides a more comprehensive understanding of their multiaxial behaviour. This enables to explore a broader spectrum of loading conditions, which is essential in real applications where loads apply in multiple directions. Moreover, the ability to integrate the testing of aged samples represents a significant advancement: it facilitates finer analysis that jointly consider the impact of ageing on the material behaviour when subjected to multiaxial loads. This, in turn, has far-reaching potential in optimizing the durability of elastomeric materials in practical engineering applications.

In the present study, we propose an extensive analysis of multiaxial mechanical tests, coupled with ageing. Particularly, we consider a carbon-black filled polychloroprene before and after thermo-oxidative ageing. The multiaxial tests are performed by means of a hexapod machine, employing two different loading paths. The discussion of the results embraces a thorough examination of kinematical fields including the evaluation of multiaxiality diversity, the impact of ageing, and the influence of loading path scaling on the fields. Subsequently, strain energy density is computed thanks to the data-driven identification algorithm, while a database containing the intrinsic material response during ageing is built. Its representation with appropriate graphical tools sheds light on the impact of ageing on multiaxial mechanical fields, for the first time in the case of a filled elastomer.

Table 1
Material formulation (in mass).

Compound	Per hundred rubber
Polychloroprene type W	100
Carbon black HAF N330	15
Sulfur	1.875
MgO	4
ZnO	5
Stearic acid	0.5
6 Phenyl-phenilenediamine	3

2. Methods

2.1. Material

Experiments are conducted on a carbon black-filled polychloroprene (15 phr) produced by *Joreau Elastomères Mélanges* (France); its formulation is given in Table 1. The material has been cured for 10 min at 170 °C and it is supplied as sheets of dimensions 250 × 250 × 2 mm^3.

Thermo-oxidative ageing is conducted in a Binder oven with forced air convection, with a precision of ±2 °C. For the purpose of this article, only one ageing condition has been considered: 21 days of exposure at 100 °C. More details about this ageing procedure are available in [18].

2.2. Experiments

In this subsection, we provide a description of the protocols followed for standard uniaxial tensile tests and complex multiaxial tests. These tests were conducted for both the unaged and the aged materials.

2.2.1. Uniaxial tensile tests

Samples are ISO-37 H3 flat dumbbell specimens, with dimensions given in the related standard [34]. The tests are performed at room temperature on a mechanical testing machine (INSTRON 5966), with use of a 10 kN load cell and a laser extensometer prescribing strain ϵ (in %). The corresponding stretch ratio λ is calculated as $\lambda = 1 + \epsilon$. The stretch rate is sufficiently low ($\dot{\lambda} = 10^{-2}$ s^{-1}) to consider the tests as quasi-static, even though consideration of the material viscoelasticity [35] should be contemplated in the future. Three samples are tested for the unaged and aged materials.

2.2.2. Multiaxial tests

2.2.2.1. Setup and samples. Multiaxial tests are conducted at room temperature on a custom test bench composed of a Breva Symétrie hexapod [36], displayed in Fig. 1a. It is made of two rigid plates: an

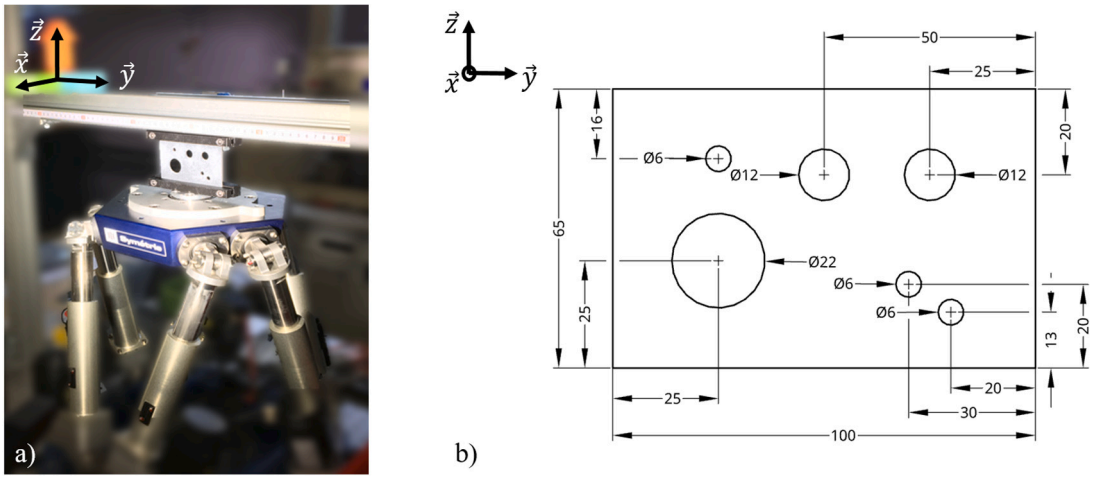

Fig. 1. (a) Homemade experimental setup: the hexapod is stretching an elastomer membrane. (b) Sample geometry with dimensions given in mm.

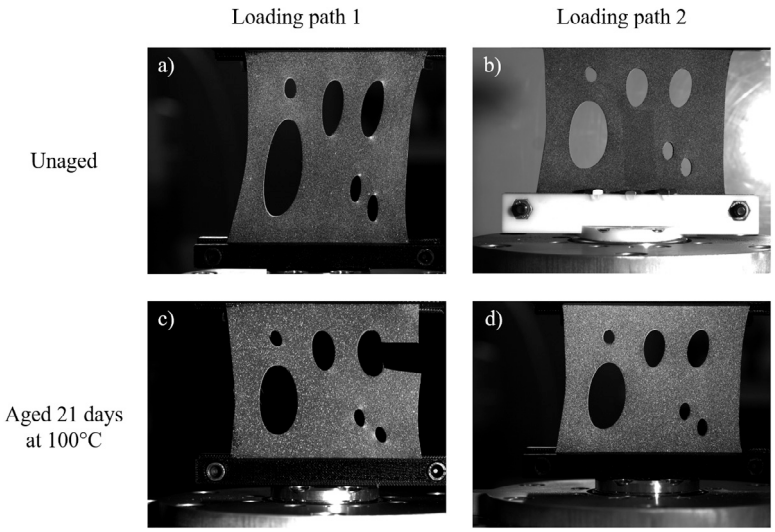

Fig. 2. Pictures of stretched specimens at the end of their respective loading path.

upper static plate and a lower mobile plate, driven by six electrical actuators. Samples are flat elastomer membranes with punchers-made circular holes, of dimensions presented in Fig. 1b. They are fixed to the setup using 3D-printed clamping jaws that have been specifically designed. A 6-axis load cell measures the resulting forces and torques for the 6 degrees of freedom. During the test, pictures of the membrane covered by a white speckle pattern are recorded by a high-resolution camera, at a frequency of 1 Hz. Image acquisition recording is synchronized with the recordings of the load cell.

2.2.2.2. Loading paths. The hexapod is displacement and rotation controlled, adhering to a prescribed input trajectory that specifies absolute positions with respect to the ones of the upper plate. The membrane lower boundary is stretched according to this trajectory, called "loading path" and denoted LP in the following. The "macroscopic" strain rate is chosen to be the same as for uniaxial tests: $\dot{\lambda} = 10^{-2}\ s^{-1}$, even though the strain rate is necessarily heterogeneous because of the heterogeneous deformation field. Both unaged and aged materials have been tested with two loading paths LP1 and LP2 detailed in Appendix A, involving only planar displacements (the two translations in the membrane plane and the rotation around its normal axis). Fig. 2 shows the final images captured for each loading path.

From Fig. 2c, it can be seen the aged material fails when undergoing LP1. This failure is due to a significant decrease in ultimate extensibility attributed to the ageing process of CR, as previously elucidated [17,18]. To prevent such sample failure, LP2 is adapted by prescribing the same trajectory but with reduced displacement amplitudes: a scaling factor of 0.41 is applied to LP1 to define LP2. This value has been determined by trial and error.

2.2.3. Post-processing

The post-processing methodology relies on successive 2D Finite Element Digital Image Correlation (FE-DIC) and Data-driven Identification (DDI) techniques. Due to the richness of multiaxial modes explored, higher numerical costs are required in comparison with standard characterizations.

- DIC is conducted from the recorded pictures using UFreckles software [37]. The result of DIC analysis is a Finite Element-interpolated displacement field, being the closest possible to the holes edges.
- From the kinematics, net forces and moment, the DDI algorithm identifies the balanced stress fields. The method is based on clusterizations of strain and stress fields, under equilibrium constraints. For further details, interested readers can refer to Appendix B.

A schematic illustration of the numerical post-processing is outlined in Fig. 3. Within this framework, we adopt the plane stress hypothesis

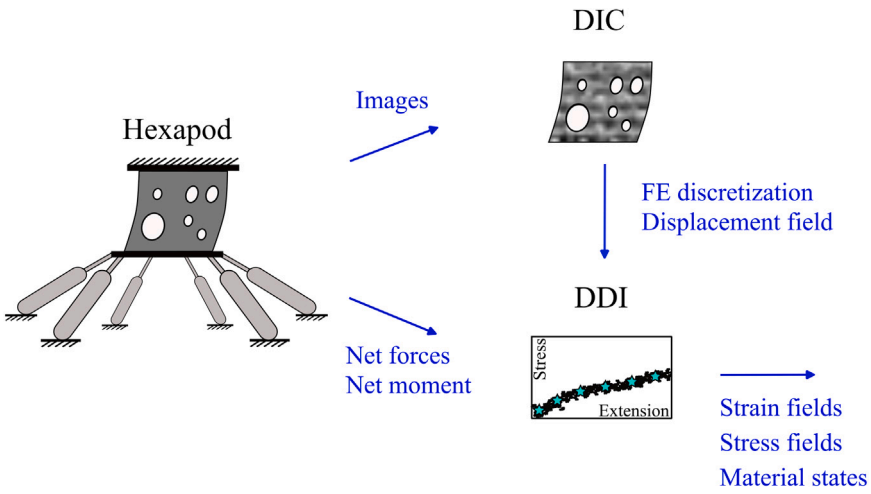

Fig. 3. Post-processing methodology, blue arrows delineate inputs and outputs at each stage.

Table 2
Optical system and parameters for the DIC (using UFreckles software) and DDI analysis.

Optical system	
Camera	Vieworks VC-50MX-M30E0
Image size	7920 × 6004 px^2
Lens	Tokina atx-i 100 mm F2.8 FF Macro
Focal lens	100 mm
Image scale	50.9 px/mm
DIC Mesh parameters	
Solver	FEM (global method)
Mesh type	Unstructured T3
Element size	70
DIC solver parameters	
Convergence limit	10^{-3}
Max iteration	50
Local normalization	ON
Sequential analysis	ON
Smoothing	OFF
DDI parameters	
Ratio $r^* = \frac{\text{number of material states}}{\text{number of mechanical states}}$	1/1000

(because the thickness of the membrane is much smaller than the in-plane dimensions), and consider the material incompressible (that implies det (**F**) = 1 and allows to compute local thickness as a function of in-plane strains). The optical system and the specific parameters selected for our analysis are detailed in Table 2.

3. Results and discussion

In this section, we present the results of the tests and investigate the relevance of this experimental framework in characterizing the multiaxial behaviour of elastomers, including the impact of ageing.

3.1. Kinematics

Through the kinematical analysis, our aim is to ensure that the material is effectively subjected to various deformation modes during the hexapod tests. Subsequently, the effects of both ageing and loading path scaling are studied.

3.1.1. Visualization in maps using the logarithm strain invariants of Criscione et al.

Graphical visualization of our kinematical data builds upon the work of Costecalde et al. [38], whose principles are recalled in this section. The DIC output is the displacement field **U**:

$$\mathbf{U} = \mathbf{x} - \mathbf{X}, \tag{1}$$

where **x** and **X** stand respectively for current and reference positions of a material point in a solid. Then, its gradient is computed to derive the deformation gradient tensor **F**:

$$\mathbf{F} = \mathbf{I} + \nabla\mathbf{U}, \tag{2}$$

with **I** the identity tensor and ∇ the gradient operator. The Hencky logarithmic strain tensor **H**, also known as true strain tensor, is

$$\mathbf{H} = \frac{1}{2}\log\left(\mathbf{F}\cdot\mathbf{F}^{\mathbf{T}}\right), \tag{3}$$

and its well-chosen invariants proposed by Criscione et al. [39] are

$$K_1 = \mathrm{tr}\,(\mathbf{H}), \quad \text{with } K_1 \in \mathbb{R}, \tag{4}$$

$$K_2 = \sqrt{\mathrm{dev}\,(\mathbf{H}) : \mathrm{dev}\,(\mathbf{H})}, \quad \text{with } K_2 > 0, \tag{5}$$

$$K_3 = 3\sqrt{6}\,\det\left(\frac{\mathrm{dev}\,(\mathbf{H})}{K_2}\right), \quad \text{with } K_3 \in [-1, 1], \tag{6}$$

where tr (.) and dev (.) respectively stand for the trace and the deviatoric operators of second order tensors. These invariants are of great relevance when dealing with multiaxial hyperelastic strain energies, as demonstrated in previous multiaxial studies for torsion [40–42], fatigue [43] and plane stress membranes [33].

K_1-invariant represents the change of volume, which is here always equal to 0 as the material is assumed incompressible. K_2 is the norm of the deviatoric part of **H**, quantifying the magnitude of strain distortion. Finally, K_3 has valuable interest for our purposes because it discriminates the strain field across deformation modes. Indeed, K_3 adopts three remarkable values for three simple deformation modes: $K_3 = 1$ for uniaxial tension (or equibiaxial compression), $K_3 = 0$ for planar tension (or simple shear), and $K_3 = -1$ for equibiaxial tension (or uniaxial compression). The computation of K_2 and K_3 invariants is made for every element of the mesh at every loading step. Fig. 4 presents a map of these invariants for each (deformed) mesh element at the final loading step of LP1 for the unaged material. It can be seen that the sample geometry induces strain concentration, gathering the highest and lowest values of K_2 around the holes. Despite a majority of elements close to uniaxial tension $K_3 \simeq 1$ at this last loading step, exploration of various deformation modes is successful.

Let us now focus on three particular mesh elements referred as I, II and III in Fig. 4. By plotting their invariants pairs on a (K_2, K_3) plane, it is possible to gather simultaneous information on both magnitude and mode of deformation. Fig. 5 shows the "invariants paths" of each element during LP1:

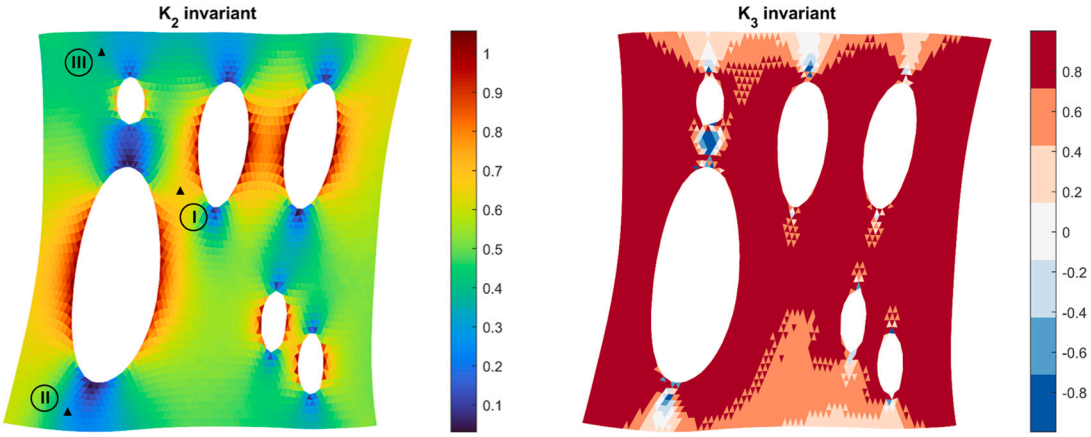

Fig. 4. Maps of invariants in the mesh at the final loading step of LP1 for the unaged material (corresponding to Fig. 2a).

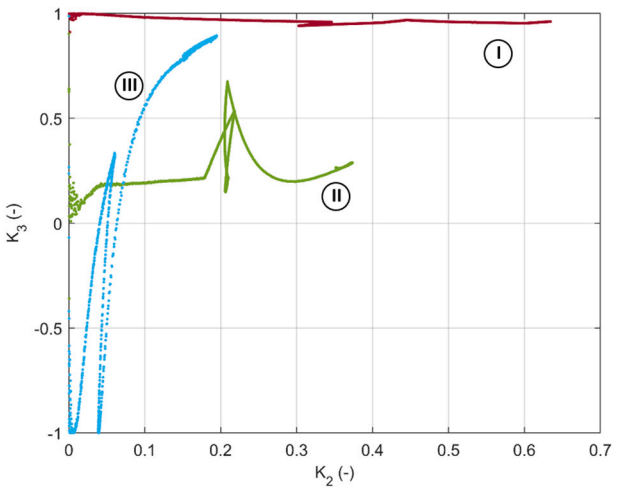

Fig. 5. Invariants paths of mesh elements I, II and III during LP1.

- Element I is very close to uniaxial tension during the whole loading history.
- Element II stays around a mixed deformation mode, around $K_3 = 0.2$, with limited variability.
- Element III switches between several modes and spans a wide range of K_3.

The analysis of the "invariants paths" from these three elements reveals different behaviours during the test. In order to understand the mechanical response at the membrane scale, it is now necessary to consider the whole mesh. Therefore, in the following, analysis throughout loading history is put aside to enable visualizations of all mesh elements, across all loading steps.

3.1.2. Diversity of multiaxiality

When considering the whole dataset, the resulting amount of data is substantial (total number of invariants pairs N_{tot} ranging between 10^6 and 10^7), and directly visualizing all pairs would result in an overloaded scatter plot. Therefore, the plane is discretized into bins, where the frequency of occurrence $f_{i,j}$ for each (K_2, K_3) pair is calculated within each $bin_{i,j}$, according to

$$f_{i,j} = \frac{1}{N_{tot}} \sum_{1}^{N_{tot}} \mathbb{1}_{(K_2,K_3) \in bin_{i,j}}. \quad (7)$$

Given the wide amplitude variation, we employ the logarithm of this frequency $\log_{10}(f)$, which is represented with a colorbar. This technique is adapted from the work of Costecalde [38]. Invariants maps for each loading path and ageing condition are represented in Fig. 6. The planes are discretized in 50 bins for K_2 in $[0, K_{2,max^a}]$, where K_{2,max^a} is the maximum invariant of map (a), and 50 bins for K_3 in $[-1, 1]$. Moreover, low occurrence values are filtered by a $10^{-4.5}$ threshold. The diversity in multiaxiality can be interpreted by assessing the scattering in K_3.

Examination of these maps reveals a majority of pairs near uniaxial tension, and a narrow range of invariants at the lowest K_3, because of the experimental difficulty to impose equibiaxial tension. Further optimizations of the samples geometry and loading paths are planned to integrate larger strain at low K_3. Yet, each map already spans the whole range of K_3 significantly, thus exploring various deformation modes. Unlike classical characterizations performed at fixed K_3, the continuous nature of these distributions demonstrates the ability to investigate mixed multiaxial strain modes, which better reflect how the material is deformed in service.

By comparing these maps one to another, the effects of ageing and of loading path scaling can be assessed; they are discussed in the following.

3.1.3. Effect of ageing

In order to understand if ageing affects the kinematics, it is essential to compare two maps obtained with the same loading path. Given the premature fracture of the sample during test (c) mentioned in

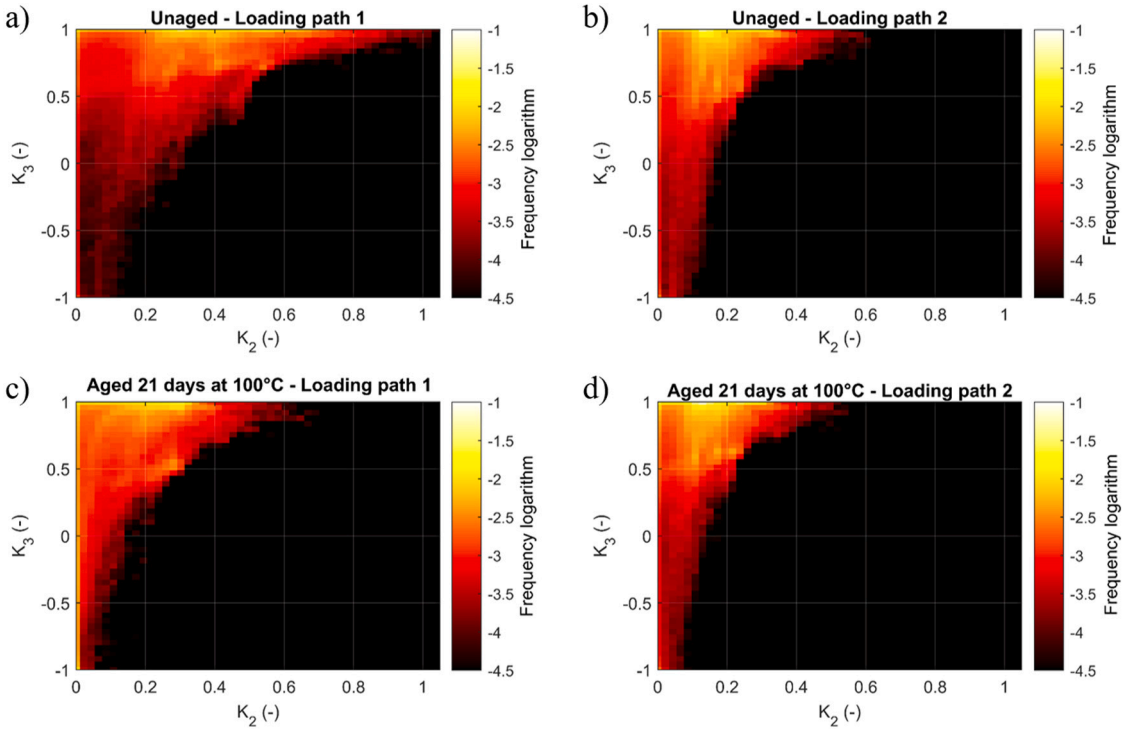

Fig. 6. Invariants maps revealing multiaxiality for two different loading paths and two different ageing conditions.

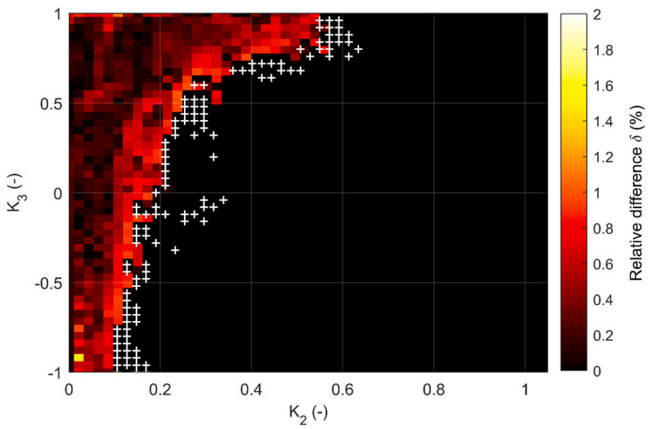

Fig. 7. Map of relative difference δ between unaged and aged maps of LP2.

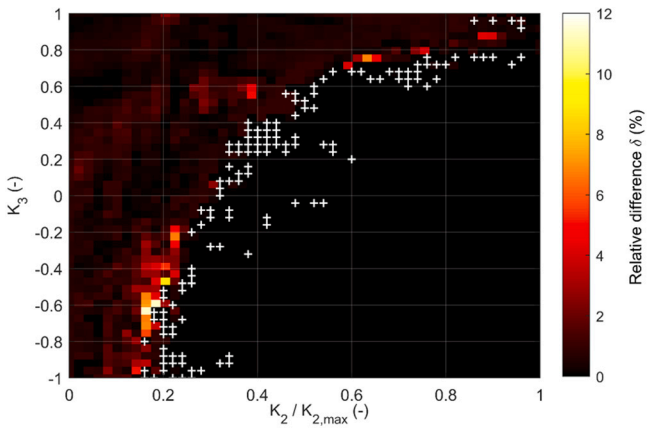

Fig. 8. Map of relative difference δ of unaged material between LP1 and LP2.

Section 2.2.2, the comparison can only be made for LP2, i.e. between maps (b) and (d) of Fig. 6. From a qualitative perspective, despite ageing-induced differences in the mechanical properties of the material, there are only minor differences between the maps in terms of both distribution and maximum value of K_2. In order to quantify the discrepancy between these maps, the following relative difference is defined:

$$\delta = \left| \frac{f_b - f_d}{f_b} \right|, \tag{8}$$

where f_b and f_d stand for the occurrence frequency in each bin of the unaged Fig. 6b and aged Fig. 6d maps, respectively. This simple indicator is useful since it provides a normalized measure, which proves beneficial when dealing with quantities of significant magnitude variation. Note that when comparing bins of maps, a mismatch can take place: one bin of map Fig. 6(b) can admit a value whereas the corresponding bin in map Fig. 6(d) is empty; these cases are indicated by a white cross. The map of the difference δ is displayed in Fig. 7.

This map exhibits an almost homogeneous distribution of the relative difference in the (K_2, K_3) plane. The maximum of δ reaches 2%, which indicates low deviation between the two maps. We observe a significant number of bin mismatches, but they correspond to large values of K_2. Because they occur infrequently, as shown in Fig. 6, their contribution should therefore be mitigated. Considering these factors, it can be inferred that there is a low influence of ageing on kinematics for a given LP.

3.1.4. Effect of loading path scaling

Let us now investigate how scaling the loading paths influences kinematics. Once again, because of the sample fracture during test (c), comparison can only be made on the unaged material between maps (a) and (b). Fig. 6 illustrates that the maximum amplitude of distortion reached during tests, $K_{2,max}$, is higher for LP1, in agreement with the larger applied displacements. When scaling the loading path, it seems that K_2 values in map Fig. 6(a) are horizontally shifted towards smaller values in map Fig. 6(b). Practically, the maps are linearly scaled for comparison, by the factor $K_2/K_{2,max}$, even if we are aware that this choice may entail some degree of oversimplification. Nevertheless, the relative difference δ is displayed in Fig. 8 in the ($K_2/K_{2,max}$, K_3) plane.

It appears that a wide majority of bins verify $\delta < 5\%$, which reflects a low deviation between scaled maps. The maximum difference, approximately 12%, is localized for large values of K_2, which also corresponds to very low frequencies that should be mitigated. Despite some mismatches at large K_2 values, the overall shape of scaled distributions for LP1 and LP2 are similar, which suggests comparable kinematic fields.

Although it should be further investigated with finer quantitative tools, the two loading paths considered in this study result in a similar kinematical response of the material. In the following, we merge the datasets of LP1 and LP2, considering solely the effect of ageing.

3.2. Strain energy density

In this section, the focus is laid on the strain energy density of the material. Results of uniaxial and multiaxial tests are reconciled using the graphical visualization tools of Section 3.1.

3.2.1. Calculation of strain energy density

As it naturally extends from uniaxial to three-dimensional formulation in the case of hyperelastic materials, the strain energy density (SED) is of great interest for our characterization to investigate the effects of ageing on the mechanical response of the material.

In the case of uniaxial tension experiments (see Section 2.2.1), SED W_{UT} is calculated by integrating the standard nominal stress–stretch ratio curve:

$$W_{UT} = \int_1^{\lambda} \frac{\sigma}{\lambda}\, d\lambda, \tag{9}$$

where σ is true stress (in MPa).

In the case of multiaxial experiments, SED is calculated for the whole strain field after post-processing of hexapod tests. For each mesh element e, at each loading step L_i, the DDI algorithm returns a mechanical state ($\mathbf{F}^e_i$, $\boldsymbol{\sigma}^e_i$) which satisfies both kinematics and equilibrium constraints. The corresponding SED W_{HEXA} is then calculated as proposed by Costecalde et al. [33].

$$W_{HEXA} = \int_0^{L_i} \boldsymbol{\sigma}^e(t) : \mathbf{D}^e(t)\, dt, \tag{10}$$

where $\boldsymbol{\sigma}$ is the true stress tensor, and $\mathbf{D}$ the strain rate tensor defined as

$$\mathbf{D} = \mathrm{sym}\left(\dot{\mathbf{F}} \cdot \mathbf{F}^{-1}\right), \tag{11}$$

with sym (.) being the symmetrization operator.

By combining hexapod tests kinematics and strain energy density, each mesh element e at each loading step L_i is characterized by the triplet (K_2, K_3, W_{HEXA}), which can be visualized in a 3D map.

3.2.2. Visualization and validation

In Fig. 9, uniaxial tensile test SED W_{UT} is represented by blue envelopes, taking deviation into account. In fact, these envelopes are only 2D in the plane (K_2, W), as the deformation mode is fixed at $K_{3=1}$. For visualizing multiaxial tests, the (K_2, K_3) horizontal plane is discretized in 50×50 bins^2 as in Fig. 6, with a colourmap indicating the

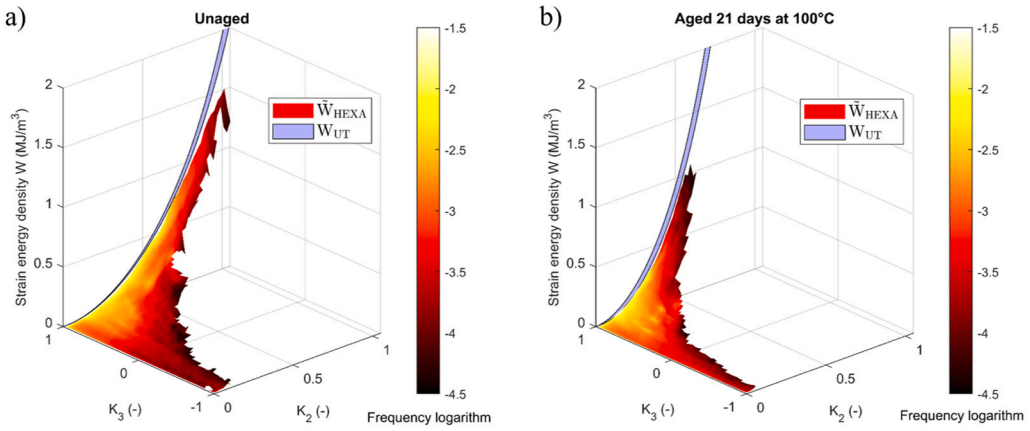

Fig. 9. Strain energy density/kinematics maps, capturing the multiaxial behaviour of CR during ageing.

occurrence frequency of invariant pairs in the bin. Then, in each bin, the mean strain energy density $\tilde{W}_{HEXA}$ of all triplets (K_2, K_3, W_{HEXA}) belonging to this bin is calculated. Supposing that a given $bin_{i,j}$ contains N elements, $\tilde{W}_{HEXA}$ is given by

$$\tilde{W}_{HEXA} = \frac{1}{N} \sum_{(K_2,K_3) \in bin_{i,j}} W_{HEXA}. \quad (12)$$

These mean values of the SED are plotted in the z-direction and the surfaces are interpolated between binned triplets.

This 3D plot visualization is proving to be a powerful tool as it highlights how kinematic distributions are retained, while capturing the quasi-static behaviour of the material for various deformation modes. Strain energy density W_{UT} and $\tilde{W}_{HEXA}$ logically increase with K_2 for both ageing conditions, as stress increases with strain magnitude. In uniaxial tension, i.e. for $K_3 = 1$, $\tilde{W}_{HEXA}$ closely aligns with W_{UT}, validating our approach for this particular deformation mode (at relatively small strain). Future investigations may prove valuable by conducting additional classical tests, such as planar tension or equibiaxial tension, to validate the dataset at other specific K_3 values.

3.2.3. *Effect of ageing*

Recalling the introduction, one of the predominant thermo-oxidative degradation mechanism in polychloroprene consists in radical chain reactions oxidizing the polymer backbone, such that new crosslinks are created in the aged material [11,12]. Consequently, the increase in crosslink density leads to the material stiffening, already observed in numerous studies [15,44], and verified for the present material thanks to standard uniaxial tensile tests [18]. In Fig. 10a, the ratio between aged and unaged SED W_{UT} is represented as a function of K_2. The SED ratio is rather uniform on the considered range, with values varying between 2 and 2.6. As $W_{UT} = 0$ in the unstretched state, the ratio becomes sensitive when K_2 approaches zero, which justifies the wide error bars.

Our attention now turns to the multiaxial results. In previous 3D maps of Fig. 9, stiffening of the material is already distinctly visible, as the concavity of the $\tilde{W}_{HEXA}$ surface is more pronounced for the aged material as compared to the unaged one. Quantitatively, a rediscretization of the aged $\tilde{W}_{HEXA}$ surface allows to calculate the ratio between multiaxial SED during ageing, represented in Fig. 10b.

In Fig. 10b, several areas of the (K_2, K_3) plane are identified:

- For $K_3 > 0.1$, a widespread uniform area is discernible with $\tilde{W}_{HEXA}$ ratio between 1.5 and 2.5, which concurs quite well with W_{UT}. In this area, the material exhibits significant strain-stiffening regardless the deformation mode, which is consistent with intuitive expectations if the isotropy of the aged material is assumed. Reconciling this map with the occurrence frequencies of Fig. 9 enables to mitigate the extreme values reached at high K_2.
- For $0.1 > K_3 > -0.5$, the ratio seems to be slightly lower. However, it is difficult to evaluate whether this difference comes from an effective drop in the $\tilde{W}_{HEXA}$ ratio, or a lack of data at this deformation modes.
- For $K_3 < -0.5$, the ratio is noisy either because of insufficient data or closeness to zero.

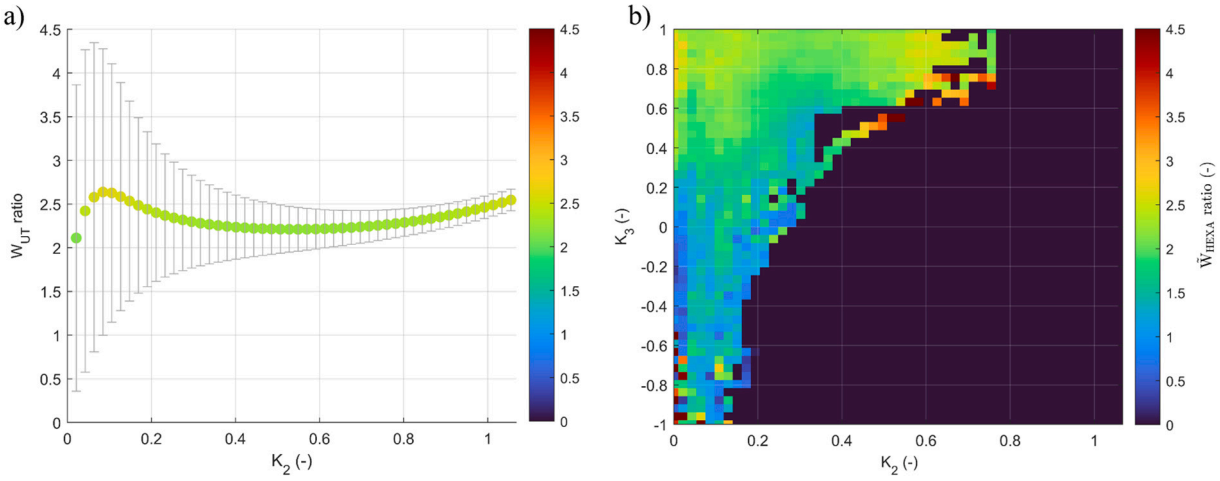

Fig. 10. (a) Ratio between aged and unaged W_{UT}, as a function of K_2. (b) Ratio between aged and unaged $\tilde{W}_{HEXA}$, as a function of K_2.

Finally, this confirms the performance of the method for characterizing the effect of ageing in a wide range of multiaxial stresses, although further verifications with additional ageing conditions could further validate the approach.

3.3. Material database

This final section aims to spotlight the material database that has been built by aggregation of experimental data. It also provides insights into potential future applications of this database.

In addition to providing the mechanical response, the DDI algorithm naturally computes and returns an intrinsic material database that samples its mechanical response [30]. Here, a sampling ratio $r^* = 1/1000$ has been chosen: one database material state samples 1000 mechanical states. By doing so, scattering and noise are reduced which facilitates data handling, at the cost of losing the loading history of each element. Quantitatively, unaged and aged databases are respectively composed of 11394 and 5394 triplets. A superimposition of such unaged and aged material databases is presented in Fig. 11.

They are formulated as functions of K_2 and K_3 invariants, as it has already been proposed for some elastomer constitutive models [45,46]. In future endeavours requiring the choice of constitutive equations, a convenient approach would involve the straightforward transformation of the material database into any strain invariants, to fit hyperelastic models. Providing data for numerous deformation modes, the present method will permit the fit of models well-suited to apprehend the multiaxial mechanical response of the material. Finally, the database sensitively captures the stiffening induced by ageing, as discussed in the above section. In the future, with more ageing conditions, it will improve the incorporation of ageing-related stiffness parameters into constitutive equations, mirroring the treatment of damage parameters [47,48].

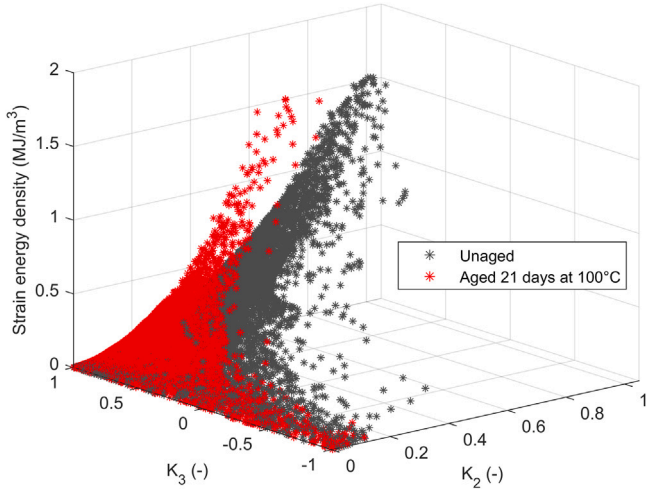

Fig. 11. Database of strain energy density and kinematic invariants scatter plots.

4. Conclusion

In the present work, a novel methodology has been proposed to characterize the multiaxial response of elastomers undergoing ageing. It has been successfully applied to a carbon-black filled polychloroprene subjected to thermo-oxidative ageing. The approach builds upon recent studies mixing sophisticated experiments, digital image correlation, and data driven identification. Emphasis has been laid on multiaxial loading conditions, in order to reach numerous modes of deformation. Presented in the form of 3D maps encompassing kinematics and strain energy density, our original multiaxial results concur remarkably well with classical uniaxial tensile tests. This consistency serves as a basis for validation with further developments potentially including the validation across other deformation modes, at larger strain levels.

A major finding of this work is the ability of the method to capture the increase in material stiffness when exposed to ageing, under multiaxial loading conditions. It has been shown that the change in strain energy density due to ageing is uniform over a wide range of deformation modes. Moreover, a database of strain energy has been built with two ageing conditions, without any modelling bias. Ongoing investigations involving additional ageing conditions aim to enrich the database, thus helping the subsequent derivation and fitting of constitutive equations, which couple ageing with the mechanical response.

CRediT authorship contribution statement

H. Madeira: Writing – review & editing, Writing – original draft, Visualization, Methodology, Investigation, Formal analysis, Data curation, Conceptualization. **L. Costecalde:** Writing – review & editing, Visualization, Software, Methodology, Data curation. **M. Coret:** Writing – review & editing, Methodology, Data curation, Conceptualization. **A. Leygue:** Writing – review & editing, Software, Methodology, Data curation, Conceptualization. **P.Y. Le Gac:** Writing – review & editing, Supervision, Conceptualization. **M. Le Gall:** Writing – review & editing, Supervision, Conceptualization. **E. Verron:** Writing – review & editing, Supervision, Methodology, Data curation, Conceptualization.

Declaration of competing interest

The authors declare that they have no known competing financial interests or personal relationships that could have appeared to influence the work reported in this paper.

Data availability

Data will be made available on request.

Acknowledgements

The authors thank Jean-Michel Lebrun for his help in 3D printing the setup claws, as well as Pierrick Guégan and Franck Pasco for their assistance in handling the experimental equipment. Gratitude is shown towards the Carnot-MERS and Ifremer for providing the funds necessary to these investigations.

Appendix A. Hexapod loading paths

The hexapod loading path LP1 is defined from the absolute position of the hexapod upper plate, as shown in Fig. A1. This path can be divided into 6 steps:

1. Vertical stretching along direction $-\vec{Z}$.
2. Horizontal stretching along direction $\vec{Y}$.
3. Simultaneous vertical stretching along $-\vec{Z}$ and in-plane rotation along $\vec{\theta_x}$.
4. Horizontal stretching along $-\vec{Y}$.
5. Simultaneous vertical stretching along $-\vec{Z}$ and in-plane rotation along $-\vec{\theta_x}$.
6. Horizontal stretching along direction $-\vec{Y}$.

Loading path LP2 is adapted by prescribing the same trajectory but with reduced displacement amplitudes, scaled by a factor 0.41. It is represented in Fig. A2.

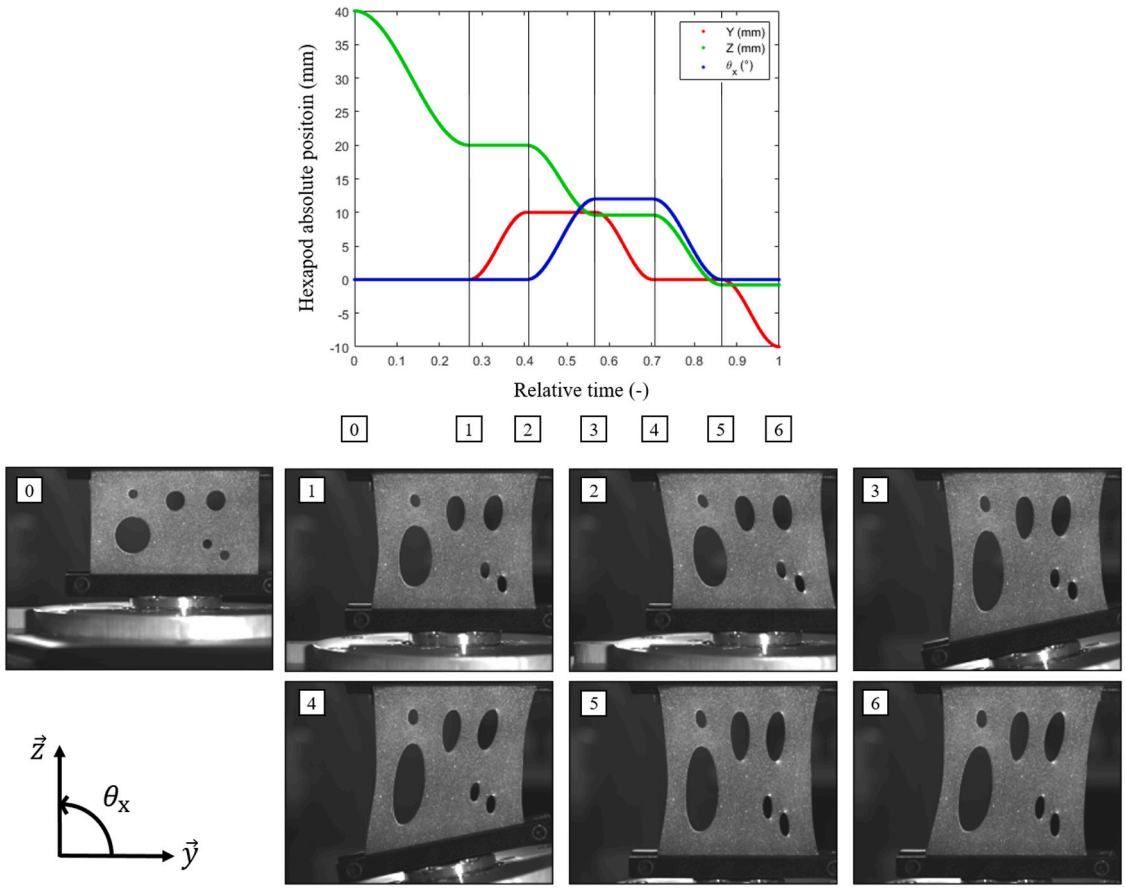

Fig. A1. Decomposition of loading path LP1.

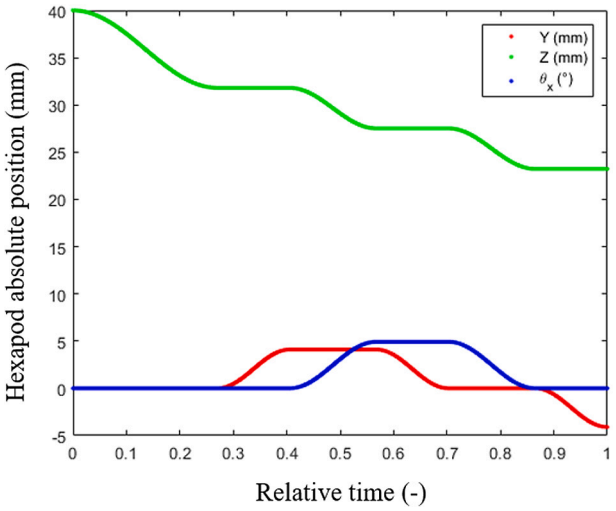

Fig. A2. Loading path LP2.

Appendix B. Data driven identification

This appendix aims to briefly recall the fundamentals of the DDI algorithm, based on [30–33,49]. The method consists in identifying an equilibrium mechanical stress field $\boldsymbol{\sigma}$, by using an extensive dataset of measured displacement fields. We consider membrane samples, which are subjected to various loading steps. From the preliminary DIC, the following quantities are known:

- A mesh.
- The displacement fields of all mesh nodes e, at all loading steps L_i.
- The resultant force, measured at one membrane boundary.

From these inputs, with a methodology detailed in [49], it is possible to calculate:

- Kinematical quantities of interest at quadrature points, such as Hencky logarithmic strain $\mathbf{H}$, or K_i-invariants.
- An equilibrium operator $\mathbf{D}$ such that $\mathbf{D}\cdot\boldsymbol{\sigma} = \boldsymbol{f}$, where $\boldsymbol{f}$ represents both the nodal forces which are equal to zero inside the mesh, and the resultant force at the boundary.

As several admissible stress fields $\boldsymbol{\sigma}$ satisfy this equation, the aim of the data-driven identification is to select a particular stress field under the principle that similar deformations yield similar stresses. A database of material stress field $\boldsymbol{\sigma}^*$ is adjusted to sample the mechanical response of the material. To do so, a clustering of the strain field $\mathbf{H}$ is made by means of a k-means algorithm, resulting in average $\mathbf{H}^*$ at the centre of their clusters. Then, $\boldsymbol{\sigma}$ is found by minimizing the loss function

$$\frac{1}{2}\sum_{e}\sum_{L_i}\|\boldsymbol{\sigma}-\boldsymbol{\sigma}^*\|_2,$$

under the constraint that $\mathbf{D}\cdot\boldsymbol{\sigma} = \boldsymbol{f}$, and where $\boldsymbol{\sigma}^*$ is the cluster average of the unknown $\boldsymbol{\sigma}$. The choice of the norm may to some extent lightly affect the numerical values of computed stress.

In practice, the minimization is carried out through a fixed point procedure, which operates as follows:

0. $\boldsymbol{\sigma}$ is chosen arbitrarily.
1. Computation of the material stress field $\boldsymbol{\sigma}^*$, such as $\boldsymbol{\sigma}^*$ is the cluster average of the mechanical stress field $\boldsymbol{\sigma}$.

2. Updating of the σ, by minimizing the distance with σ^* under equilibrium constrains $\mathbf{D} \cdot \sigma = f$.
3. Unless convergence is reached, back to step 1.

References

[1] J.W. Fox, N.C. Goulbourne, On the dynamic electromechanical loading of dielectric elastomer membranes, J. Mech. Phys. Solids 56 (2008) 2669–2686, http://dx.doi.org/10.1016/j.jmps.2008.03.007.

[2] D. Ahmad, R.M. Ajaj, M. Amoozgar, Elastomer-based skins for morphing aircraft applications: Effect of biaxial strain rates and prestretch, Polym. Test. 113 (2022) 107655, http://dx.doi.org/10.1016/j.polymertesting.2022.107655.

[3] T. Grelle, D. Wolff, M. Jaunich, Temperature-dependent leak tightness of elastomer seals after partial and rapid release of compression, Polym. Test. 48 (2015) 44–49, http://dx.doi.org/10.1016/j.polymertesting.2015.09.009.

[4] R.Q. Luo, Impact simulation and experiment on rubber anti-vibration systems, Polym. Test. 50 (2016) 335–342, http://dx.doi.org/10.1016/j.polymertesting.2016.02.001.

[5] A. Azoug, A. Thorin, R. Nevière, R.-M. Pradeilles-Duval, A. Constantinescu, Influence of orthogonal prestrain on the viscoelastic behaviour of highly-filled elastomers, Polym. Test. 32 (2013) 375–384, http://dx.doi.org/10.1016/j.polymertesting.2012.12.005.

[6] S.Y. Ch'ng, A. Andriyana, E. Verron, O. Kahbasi, R. Ahmad, Development of a novel experimental device to investigate swelling of elastomers in biodiesel undergoing multiaxial large deformation, Exp. Mech. 53 (2013) 1323–1332, http://dx.doi.org/10.1007/s11340-013-9737-2.

[7] J.R. Shelton, Aging and oxidation of elastomers, Rubber Chem. Technol. 30 (1957) 1251–1290, http://dx.doi.org/10.5254/1.3542760.

[8] J.I. Cunneen, Oxidative aging of natural rubber, Rubber Chem. Technol. 41 (1968) 182–208, http://dx.doi.org/10.5254/1.3539169.

[9] M. Tayefi, M. Eesaee, M. Hassanipour, S. Elkoun, E. David, P. Nguyen-Tri, Recent progress in the accelerated aging and lifetime prediction of elastomers : A review, Polym. Degrad. Stab. 214 (2023) 110379, http://dx.doi.org/10.1016/j.polymdegradstab.2023.110379.

[10] K. Bensalem, M. Eesaee, M. Hassanipour, S. Elkoun, E. David, K. Agbossou, P. Nguyen-Tri, Lifetime estimation models and degradation mechanisms of elastomeric materials: A critical review, Polym. Degrad. Stab. 220 (2023) 110644, http://dx.doi.org/10.1016/j.polymdegradstab.2023.110644.

[11] F. Delor, J. Lacoste, J. Lemaire, N. Barrois-Oudin, C. Cardinet, Photo- and thermal ageing of polychloroprene: Effect of carbon black and crosslinking, Polym. Degrad. Stab. 53 (1996) 361–369, http://dx.doi.org/10.1016/0141-3910(96)00097-3.

[12] Y. Miyata, M. Atsumi, Spectroscopic studies on the initial stages of thermal degradation of polychloroprene, J. Polym. Sci. A 26 (1988) 2561–2572, http://dx.doi.org/10.1002/pola.1988.080260925.

[13] R. Bouaziz, L. Truffault, R. Borisov, C. Ovalle, L. Laiarinandrasana, G. Miquelard-Garnier, B. Fayolle, Elastic properties of polychloroprene rubbers in tension and compression during ageing, Polymers 12 (2020) 2354, http://dx.doi.org/10.3390/polym12102354.

[14] M. Nait Abdelaziz, G. Ayoub, X. Colin, M. Benhassine, M. Mouwakeh, New developments in fracture of rubbers: Predictive tools and influence of thermal aging, Int. J. Solids Struct. 165 (2019) 127–136, http://dx.doi.org/10.1016/j.ijsolstr.2019.02.001.

[15] P.-Y. Le Gac, M. Celina, G. Roux, J. Verdu, P. Davies, B. Fayolle, Predictive ageing of elastomers: Oxidation driven modulus changes for polychloroprene, Polym. Degrad. Stab. 130 (2016) 348–355, http://dx.doi.org/10.1016/j.polymdegradstab.2016.06.014.

[16] Y.T. Wei, L. Nasdala, H. Rothert, Z. Xie, Experimental investigations on the dynamic mechanical properties of aged rubbers, Polym. Test. 23 (2004) 447–453, http://dx.doi.org/10.1016/j.polymertesting.2003.09.006.

[17] P.-Y. Le Gac, P.-A. Albouy, B. Fayolle, J. Verdu, Relationship between macromolecular network and fatigue properties of unfilled polychloroprene rubber, Polym. Degrad. Stab. 192 (2021) 109669, http://dx.doi.org/10.1016/j.polymdegradstab.2021.109669.

[18] H. Madeira, P.-Y. Le Gac, M. Le Gall, E. Verron, Prediction of fatigue lifetime by the strain energy density for filled polychloroprene during thermo-oxidative ageing, Int. J. Fatigue 178 (2024) 108023, http://dx.doi.org/10.1016/j.ijfatigue.2023.108023.

[19] J.-B. Le Cam, B. Huneau, E. Verron, Fatigue damage in carbon black filled natural rubber under uni- and multiaxial loading conditions, Int. J. Fatigue 52 (2013) 82–94, http://dx.doi.org/10.1016/j.ijfatigue.2013.02.022.

[20] N. Saintier, G. Cailletaud, R. Piques, Crack initiation and propagation under multiaxial fatigue in a natural rubber, Int. J. Fatigue 28 (2006) 61–72, http://dx.doi.org/10.1016/j.ijfatigue.2005.03.006.

[21] J.L. Poisson, S. Méo, F. Lacroix, G. Berton, M. Hosséini, N. Ranganathan, Comparison of fatigue criteria under proportional and non-proportional multiaxial loading, Rubber Chem. Technol. 91 (2018) 320–338, http://dx.doi.org/10.5254/rct.18.82696.

[22] L.R.G. Treloar, Stress-strain data for vulcanized rubber under various types of deformation, Rubber Chem. Technol. 17 (1944) 813–825, http://dx.doi.org/10.5254/1.3546701.

[23] S. Kawabata, M. Matsuda, K. Tei, H. Kawai, Experimental survey of the strain energy density function of isoprene rubber vulcanizate, Macromolecules 14 (1981) 154–162, http://dx.doi.org/10.1021/ma50002a032.

[24] M.C. Boyce, E.M. Arruda, Constitutive models of rubber elasticity: A review, Rubber Chem. Technol. 73 (2000) 504–523, http://dx.doi.org/10.5254/1.3547602.

[25] L. Bernardi, R. Hopf, A. Ferrari, A.E. Ehret, E. Mazza, On the large strain deformation behavior of silicone-based elastomers for biomedical applications, Polym. Test. 58 (2017) 189–198, http://dx.doi.org/10.1016/j.polymertesting.2016.12.029.

[26] G. Marckmann, E. Verron, Comparison of hyperelastic models for rubber-like materials, Rubber Chem. Technol. 79 (2006) 835–858, http://dx.doi.org/10.5254/1.3547969.

[27] H. He, Q. Zhang, Y. Zhang, J. Chen, L. Zhang, F. Li, A comparative study of 85 hyperelastic constitutive models for both unfilled rubber and highly filled rubber nanocomposite material, Nano Mater. Sci. 4 (2022) 64–82, http://dx.doi.org/10.1016/j.nanoms.2021.07.003.

[28] A. Anssari-Benam, A. Bucchi, A generalised neo-Hookean strain energy function for application to the finite deformation of elastomers, Int. J. Non-Linear Mech. 128 (2021) 103626, http://dx.doi.org/10.1016/j.ijnonlinmec.2020.103626.

[29] A. Anssari-Benam, A. Horgan, A three-parameter structurally motivated robust constitutive model for isotropic incompressible unfilled and filled rubber-like materials, Eur. J. Mech. A Solids 95 (2022) 104605, http://dx.doi.org/10.1016/j.euromechsol.2022.104605.

[30] A. Leygue, M. Coret, J. Réthoré, L. Stainier, E. Verron, Data-based derivation of material response, Comput. Methods Appl. Mech. Engrg. 331 (2018) 184–196, http://dx.doi.org/10.1016/j.cma.2017.11.013.

[31] A. Leygue, R. Seghir, J. Réthoré, M. Coret, E. Verron, L. Stainier, Non-parametric material state field extraction from full field measurements, Comput. Mech. 64 (2019) 501–509, http://dx.doi.org/10.1007/s00466-019-01725-z.

[32] M. Dalémat, M. Coret, A. Leygue, E. Verron, Measuring stress field without constitutive equation, Mech. Mater. 136 (2019) 103087, http://dx.doi.org/10.1016/j.mechmat.2019.103087.

[33] L. Costecalde, A. Leygue, M. Coret, E. Verron, Data-driven identification of hyperelastic models by measuring the strain energy density field, Rubber Chem. Technol. 96 (2023) 443–454, http://dx.doi.org/10.5254/rct-23.386903.

[34] ISO37:2005, Rubber, Vulcanized Or Thermoplastic — Determination of Tensile Stress–Strain Properties, Tech. Rep., ISO, Switzerland, 2015.

[35] V.P. Privalko, S.M. Ponomarenko, E.G. Privalko, F. Schön, W. Gronski, Thermoelasticity and stress relaxation behavior of polychloroprene/organoclay nanocomposites, Eur. Polym. 41 (2005) 3042–3050, http://dx.doi.org/10.1016/j.eurpolymj.2005.06.011.

[36] M. Dalémat, Une Expérimentation Réussie Pour L'identification De La Réponse Mécanique Sans Loi De Comportement: Approche Data-Driven Appliquée Aux Membranes Élastomères (Thèse de doctorat), 2019, tel-02506891v2.

[37] J. Réthoré, Ufreckles (v 2.0), 2018, http://dx.doi.org/10.5281/zenodo.1433776, Zenodo.

[38] L. Costecalde, Data-Driven Model Identification for Hyperelasticity: Mapping the Strain Energy Throughout Multiaxial Experiments (Thèse de doctorat), 2023.

[39] J.C. Criscione, J.D. Humphrey, A.S. Douglas, W.C. Hunter, An invariant basis for natural strain which yields orthogonal stress response terms in isotropic hyperelasticity, J. Mech. Phys. Solids 48 (2000) 2445–2465, http://dx.doi.org/10.1016/S0022-5096(00)00023-5.

[40] A.-S. Lectez, E. Verron, B. Huneau, How to identify a hyperelastic constitutive equation for rubber-like materials with multiaxial tension–torsion experiments, Int. J. Non-Linear Mech. 65 (2014) 260–270, http://dx.doi.org/10.1016/j.ijnonlinmec.2014.06.007.

[41] D. Prasad, K. Kannan, An analysis driven construction of distortional-mode-dependent and hill-stable elastic potential with application to human brain tissue, J. Mech. Phys. Solids 134 (2020) 103752, http://dx.doi.org/10.1016/j.jmps.2019.103752.

[42] V. Kulwant, K. Arvind, D. Prasad, P. Sreejith, K.V. Mohankumar, K. Kannan, A semi-analytical inverse method to obtain the hyperelastic potential using experimental data, J. Mech. Phys. Solids 181 (2023) 105431, http://dx.doi.org/10.1016/j.jmps.2023.105431.

[43] E. Le Mire, E. Verron, B. Huneau, N. Selles, Multiaxial fatigue experiments for elastomers based on true strain invariants, J. Rubber Res. 24 (2021) 227–236, http://dx.doi.org/10.1007/s42464-021-00088-6.

[44] M. Celina, J. Wise, D. Ottesen, K. Gillen, R. Clough, Correlation of chemical and mechanical property changes during oxidative degradation of neoprene, Polym. Degrad. Stab. 68 (2000) 171–184, http://dx.doi.org/10.1016/S0141-3910(99)00183-4.

[45] P.A. Kakavas, A new development of the strain energy function for hyperelastic materials using a logarithmic strain approach, Appl. Polym. Sci. 77 (2000) 660–672, http://dx.doi.org/10.1002/(SICI)1097-4628(20000718)77:3%3C660::AID-APP21%3E3.0.CO;2-A.

[46] H. Xiao, An explicit, direct approach to obtaining multiaxial elastic potentials that exactly match data of four benchmark tests for rubbery materials—part 1: Incompressible deformations, Acta Mech. 223 (2012) 2039–2063, http://dx.doi.org/10.1007/s00707-012-0684-2.

[47] R. Kadri, M. Nait Abdelaziz, B. Fayolle, M. Ben Hassine, J.-F. Witz, A unified mechanical based approach to fracture properties estimates of rubbers subjected to aging, Int. J. Solids Struct. 234-235 (2022) 111305, http://dx.doi.org/10.1016/j.ijsolstr.2021.111305.

[48] A. Bahrololoumi, V. Morovati, M. Shaafaey, R. Dargazany, A multi-physics approach on modeling of hygrothermal aging and its effects on constitutive behavior of cross-linked polymers, J. Mech. Phys. Solids (2021) 104614, http://dx.doi.org/10.1016/j.jmps.2021.104614.

[49] M. Dalémat, M. Coret, A. Leygue, E. Verron, Robustness of the data-driven identification algorithm with incomplete input data, J. Theoret. Comput. Appl. Mech. (2024) 12590, http://dx.doi.org/10.46298/jtcam.12590.